

Revealing the state space of turbulence using machine learning

Jacob Page^{1,2}, Michael P. Brenner^{3,4} & Rich R. Kerswell²

¹*School of Mathematics, University of Edinburgh, Edinburgh, EH9 3FD, UK*

²*DAMTP, Centre for Mathematical Sciences, University of Cambridge, Cambridge, CB3 0WA, UK*

³*School of Engineering and Applied Sciences, Harvard University, Cambridge MA 02138*

⁴*Google Research, Mountain View, CA 94043*

Despite the apparent complexity of turbulent flow, identifying a simpler description of the underlying dynamical system remains a fundamental challenge. Capturing how the turbulent flow meanders amongst unstable states (simple invariant solutions) in phase space as envisaged by Hopf in 1948 using some efficient representation offers the best hope of doing this, despite the inherent difficulty in identifying these states. Here, we use machine learning to make a significant step towards this goal by demonstrating that deep convolutional autoencoders can identify low-dimensional representations of two-dimensional turbulence which are closely associated with the simple invariant solutions characterizing the turbulent attractor. To establish this, we develop *latent Fourier analysis* that decomposes the flow embedding into a set of orthogonal latent Fourier modes which decode into physically meaningful patterns resembling simple invariant solutions. The utility of this approach is highlighted by analysing turbulent Kolmogorov flow (flow on a 2D torus forced at large scale) at $Re = 40$ where, in between intermittent bursts, the flow resides in the neighbourhood of an unstable state and is very low dimensional. Latent Fourier analysis is found to be a far more efficient detector of periodic orbits buried with the turbulence than the current state of the art.

Building effective low-order representations of turbulent flows is a long-standing challenge that could dramatically improve our capabilities for prediction and control. Current state-of-the-art techniques for low-order modelling typically involve constructing a set of orthogonal ‘modes’ from a dataset. Perhaps most well known is principal component analysis (PCA), which produces an orthogonal basis to optimally represent the training snapshots. However, while highly interpretable, modes in the basis may have little dynamical significance individually¹, and other methods that attempt to also infer dynamics – for example dynamic mode decomposition² – are ill-suited to chaotic systems like turbulence³. The failure of these low-order representations to faithfully reconstruct even weak turbulence contrasts with the dynamical systems view of the flow, in which turbulence is understood to arise as the structure of phase state complexifies under increasing Reynolds number, Re^{4-8} . In this framework, a turbulent flow is considered as a long nonclosing orbit in a high-dimensional state space, transiting between unstable simple invariant solutions which are the ‘building blocks’ of the chaotic attractor⁵. Such a viewpoint suggests that there are efficient low-order representations of the flow which are rooted in the underlying simple invariant solutions, though the nonlinearity of the Navier-Stokes equations confounds our attempts

to hand-craft a solution.

The recent emergence of deep convolutional neural networks (CNNs) represents an opportunity to identify such representations due to their ability to extract patterns^{9,10} that can result in highly efficient low-dimensional embeddings of complex data. The utility of CNNs in the study of nonlinear partial differential equations (PDEs) has been demonstrated recently in a number of canonical examples, where their accurate parameterisation of the solution manifold has been exploited to successfully predict chaotic dynamics for multiple Lyapunov times¹¹, to estimate the dimension of chaotic attractors¹² and to design new spatial discretisation schemes¹³.

Using a CNN to decompose a turbulent flow into a series of recurrent spatial *patterns* should be contrasted to a projection onto a hand-crafted orthogonal basis such as Fourier modes, where the coupling of all wavenumbers through the nonlinearity of the Navier-Stokes equation renders individual modes dynamically insignificant. A learnt basis has the potential to encode and parameterise the alphabet of dynamical processes present, though at a loss of physical interpretability. Here we show how the presence of a continuous symmetry in the physical system can be exploited to perform a decomposition of embeddings of a turbulent flow in latent space. This *latent* Fourier analysis – analogous to a Fourier decomposition in physical space – yields a (latently) orthogonal basis of recurrent patterns that exhibit striking resemblance to simple invariant solutions of the underlying dynamical system.

Dimensionality reduction of Kolmogorov flow

We use deep CNNs to build efficient low-dimensional representations of snapshots from a computation of monochromatically forced, two-dimensional turbulence on a doubly-periodic square $[0, 2\pi] \times [0, 2\pi]$. In two dimensions the Navier-Stokes equations can be combined and written concisely in terms of the out-of-plane vorticity $\omega := (\nabla \times \mathbf{u}) \cdot \hat{\mathbf{z}}$,

$$\partial_t \omega + \mathbf{u} \cdot \nabla \omega = \frac{1}{Re} \nabla^2 \omega + (\nabla \times \mathbf{f}) \cdot \hat{\mathbf{z}}, \quad (1)$$

where $\mathbf{f} = \sin 4y \hat{\mathbf{x}}$ (‘Kolmogorov’ flow¹⁴ with the specific choice of four forcing wavelengths in the square^{15,16}). There are a number of symmetries, the most important in the context of this work being the continuous translational symmetry $\mathcal{T}_s : \omega(x, y) \rightarrow \omega(x + s, y)$. There is also a discrete shift-reflect symmetry $\mathcal{S} : \omega(x, y) \rightarrow -\omega(-x, y + \pi/4)$ and a rotational symmetry $\mathcal{R} : \omega(x, y) \rightarrow \omega(-x, -y)$. Throughout we hold the Reynolds number fixed at $Re = 40$, where a large number of simple invariant solutions have been found¹⁶.

We seek efficient low-dimensional *embeddings* $\{\mathcal{E}\}$ of vorticity snapshots $\{\omega\}$, which are essentially greyscale images of dimension $N_x \times N_y = 128 \times 128$. To do this we construct deep CNNs in the form of autoencoders, which are trained to reconstruct the input snapshots with dimension reduction applied as part of the network structure. The specific architectures we use are

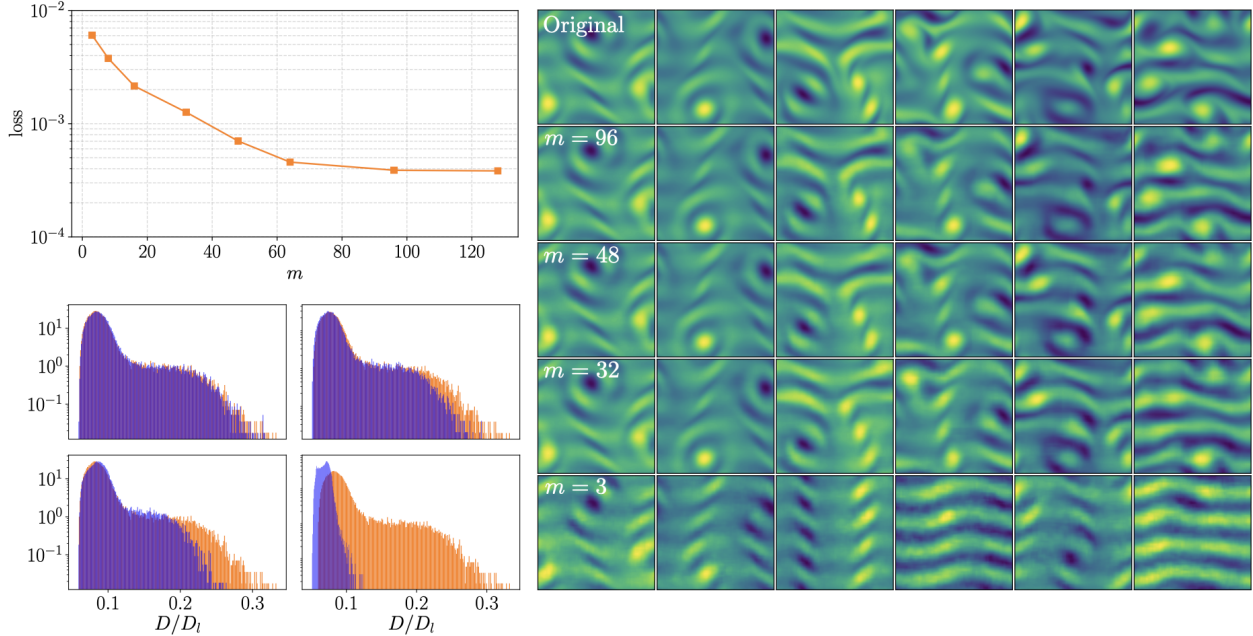


Figure 1: **Autoencoders for dimensionality reduction in Kolmogorov flow.** (Top left) Loss $\frac{1}{|\text{data}|} \sum_{\text{data}} \|[\mathcal{D} \circ \mathcal{E}](\omega) - \omega\|_2^2$ as a function of embedding dimension m . (Bottom left) Dissipation PDFs of autoencoded vorticity fields. The background orange is obtained from the original test dataset, the overlaid blue PDFs are for $m \in \{96, 48, 32, 3\}$ (top left to bottom right). (Right) Decodes of a set of snapshots of increasing dissipation for various embedding dimensions m . Snapshots are ordered left-to-right by dissipation, running from $D/D_l \approx 0.08$ to $D/D_l \approx 0.26$ indicating, for example, that $m = 3$ captures low-dissipation episodes well but struggles to represent high-dissipation events.

described in detail in Methods, but all consist of an encoder module, $\mathcal{E}: \mathbb{R}^{128 \times 128} \rightarrow \mathbb{R}^m$ – a series of five convolutional layers with pooling to reduce the dimension from 128^2 to 128 – followed by fully connected layers to further reduce the dimension to $m \leq 128$ (the “embedding”). A similar structure is used to decode the embeddings, $\mathcal{D}: \mathbb{R}^m \rightarrow \mathbb{R}^{128 \times 128}$, and the weights that define these functions are obtained by performing stochastic gradient descent on the loss functional $\frac{1}{|\text{data}|} \sum_{\text{data}} \|[\mathcal{D} \circ \mathcal{E}](\omega) - \omega\|_2^2$. Further details on the training dataset and the numerics are provided in Methods.

The impact of autoencoder dimension on the fidelity of the reconstruction $[\mathcal{D} \circ \mathcal{E}](\omega)$ is examined in figure 1. The loss drops monotonically with increasing m , with even very low dimensional networks (e.g. $m = 3$) displaying relatively small losses (two unrelated vorticity fields typically yield an $O(1)$ loss), which suggests that much of the underlying dynamical system may be low dimensional. Furthermore, networks with modest m (e.g. see the PDF for $m = 32$ in figure 1) retain much of the high-dissipation tail in PDFs of $D := \langle (\nabla \mathbf{u})^2 \rangle_V = \langle \omega^2 \rangle_V$. This indicates a retention of smaller scales and sharp variations in ω under dimensionality reduction, in contrast to

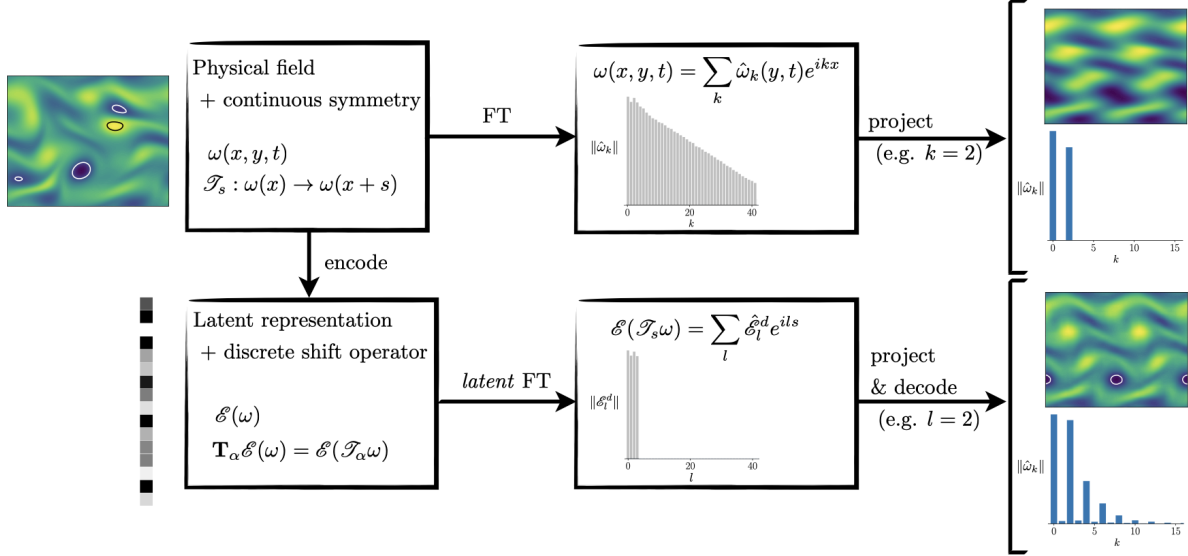


Figure 2: **An overview of the approach to performing latent Fourier decompositions on (latent) representations of physical systems with a continuous symmetry.** A latent Fourier decomposition is performed by constructing an operator to map between embeddings of shifted versions of the same snapshot. Note that only four latent wavenumbers, $\{0, 1, 2, 3\}$, are required for the monochromatically forced turbulence considered here. In the “project and decode” step (bottom right) the projection within the $l = 0$ subspace is also included (see the discussion in the text). For comparison, the projection onto $k = 0$ is also included in the projection onto the physical Fourier modes.

standard techniques like PCA. Even at $m = 3$, the accurate reproductions of low dissipation events (see the snapshots in figure 1) contain the full spectrum of Fourier modes.

To examine how these networks can reduce the dimensionality of the data while retaining a broad spectrum of lengthscales, we describe a method for decomposing the latent representations of vortical snapshots into a finite set of recurrent patterns which can be visualised individually.

Latent Fourier analysis

The continuous translational symmetry in the governing equation (1) and boundary conditions provides a mechanism to decompose the latent embeddings of the vorticity fields into recurrent ‘patterns’ that reveal the structure of the latent space. This decomposition is analogous to a Fourier transform in physical space, $\omega(x, y, t) = \sum_{k \in \mathbb{Z}} \hat{\omega}_k(y, t) \exp(ikx)$. However, the autoencoder representations encode horizontal position x in an unknown way. To perform a similar decomposition for embeddings, we first must construct an operator that can map between an embedding of a snapshot and an embedding of a shifted version of the same field: $\mathbf{T}_\alpha \mathcal{E}(\omega) = \mathcal{E}(\mathcal{T}_\alpha \omega)$, where the fixed shift $\alpha \in (0, 2\pi)$ is a design choice. This procedure applied to the vorticity field itself would result

in a numerical approximation to a Fourier transform through the eigenvalues and eigenvectors of \mathbf{T}_α , with a maximum resolved wavenumber set by the Nyquist condition, $k_{max} = \pi/\alpha$. For the embeddings, \mathcal{E} , the value of α sets a maximum *latent* wavenumber that can be resolved, l_{max} . As we will show below, the required latent resolution is considerably coarser than the smallest scales generated by the governing PDE (1).

To see the connection to a standard Fourier transform, consider a discrete shift $\alpha = 2\pi/n$, with $n \in \mathbb{N}$. By design, $\mathbf{T}_\alpha^n \mathcal{E}(\omega) = \mathcal{E}(\omega)$, so the eigenvalues of \mathbf{T}_α are $\Lambda_j = \exp(2\pi i l_j/n)$, with $l_j \in \mathbb{Z}$. We assume that the value of α has been chosen small enough so that no l_j are found beyond a maximum (l_{max}). With this, approximations to continuous shifts s of an embedding $\mathcal{E}(\omega)$ are

$$\mathcal{E}(\mathcal{T}_s \omega) = \sum_l \left(\sum_{j=0}^{d(l)-1} \mathcal{P}_j^l(\mathcal{E}(\omega)) \right) e^{ils} := \sum_l \left(\sum_{j=0}^{d(l)-1} [(\boldsymbol{\xi}_j^{\dagger(l)})^H \mathcal{E}(\omega)] \boldsymbol{\xi}_j^{(l)} \right) e^{ils}. \quad (2)$$

Here l is the *latent wavenumber* and the operator \mathcal{P}_j^l is a projector in direction j within the eigenspace of wavenumber l , which has geometric multiplicity $d(l)$. Unlike physical Fourier modes, the latent wavenumbers are degenerate. In equation (2) we have assumed that some bi-orthogonal basis has been constructed; a specific choice is discussed further below.

The number of required latent wavenumbers and their degeneracy provides insight into the nonlinear interactions in physical space. Each latent Fourier mode of wavenumber l can be decoded into a $2\pi/l$ -periodic pattern which has a physical Fourier decomposition projecting onto wavenumbers $k_q = ql$, $q \in \mathbb{N}$ (see the example in the schematic of figure 2). These recurrent patterns represent pathways through physical Fourier wavenumbers which are selected by the dynamics.

To perform a latent Fourier decomposition within our autoencoder, we build a shift operator using a least-squares fit to find a \mathbf{T}_α that maps between embeddings of the test set and embeddings of the same vorticity fields shifted by α in x (see Methods). Numerical experiments reducing α reveal a maximum latent wavenumber $l_{max} = 3$ for embeddings $m \geq 32$. This truncation suggests that the learnt representations can be decomposed into a set of recurrent patterns which are at most $2\pi/3$ -periodic. The energy in all higher physical wavenumbers, $k > 3$, is assigned during the decode of this coarse set of features in the latent space (e.g. $k = 5$ can only be encoded into $l = 1$ and $k = 8$ into $l = 2$). An example eigenvalue spectrum for the $m = 96$ network is reported in figure 3, the (degenerate) eigenvalues lying approximately on $l \in \{0, 1, 2, 3\}$. Some example $2\pi/l$ -periodic physical patterns associated with a particular value of l are displayed alongside the spectrum. These images were generated by projecting the embedding of a snapshot onto the relevant eigenspace and decoding the result. Note that, in contrast to a standard Fourier transform, the $l = 0$ contribution must always be included for the decode operation to yield a physical field. Projections onto the $l = 0$ subspace decode to horizontal stripes of vorticity which align with the (curl of) the forcing in equation (1); the vorticity amplitude of each stripe is distorted by the $l > 0$ modes into vortical features. In this way, much of the y -dependence in the final decoded snapshot

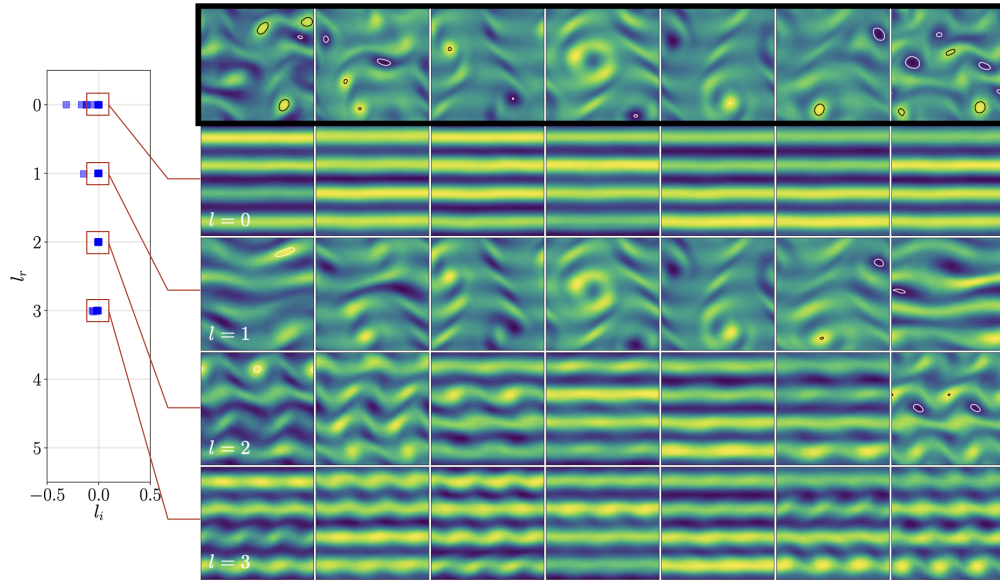


Figure 3: **Eigenvalue spectra of a latent symmetry operator and decodes of the projection onto individual eigenspaces for example snapshots.** (Left) Eigenvalue spectrum of \mathbf{T}_α on the $m = 96$ autoencoder with $\alpha = 2\pi/9$. Note that only half the spectrum is shown. (Right) Seven example snapshots (top row, inside black box) and the decodes of the projection of their embeddings onto individual latent Fourier eigenspaces. Note that the $l = 0$ subspace is always included for decodes of latent wavenumbers $l > 0$.

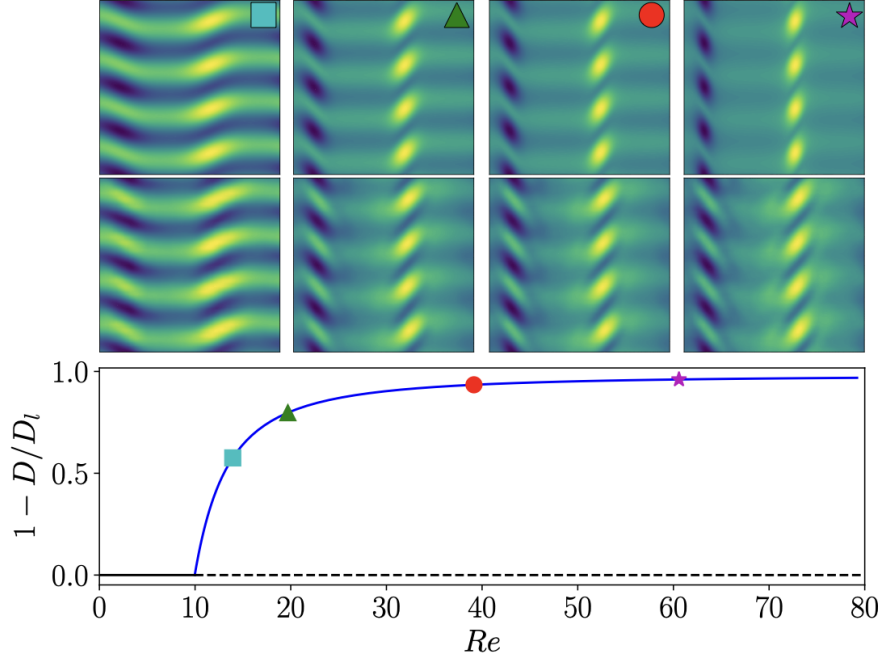


Figure 4: **The primary bifurcation of Kolmogorov flow and its connection to the primary latent Fourier mode within the $l = 1$ subspace.** (Top) Equilibrium states at $Re \approx \{14, 20, 40, 60\}$ from the solution branch which bifurcates from the basic laminar state at $Re \approx 9.97$. (Middle) Decode of the projection of the embeddings of these equilibria onto the first PCA modes within the $l = 0$ and $l = 1$ subspaces. (Bottom) Amplitude (measured by dissipation) of this equilibrium as a function of Reynolds number (blue line, the laminar solution sits on $1 - D/D_l = 0$) with the example states shown above identified with symbols. It should be emphasised that training has been conducted at fixed $Re = 40$, and that all of the training snapshots are from within the turbulent attractor and do not feature this simple equilibrium.

is controlled by the $l = 0$ subspace.

The decodes in figure 3 for $l > 0$ have the expected periodicity, $\mathcal{F}_{2\pi/l}[\mathcal{D}(\sum_j \mathcal{P}_j^l(\mathcal{E}))] = \mathcal{D}(\sum_j \mathcal{P}_j^l(\mathcal{E}))$. In contrast to a projection onto individual Fourier modes in physical space, the projection onto individual latent wavenumbers produces patterns with vortical features that can be clearly identified in the original snapshots. The wide range of features observed in decodes of individual latent wavenumbers is possible due to the degeneracy of the eigenspaces, which we now discuss.

Connections to simple invariant solutions

The degenerate set of recurrent patterns encoded within each latent eigenspace can be revealed by an appropriate choice of basis to define the projectors \mathcal{P}_j^l in equation (2). We have found PCA

within each eigenspace to be robust for this purpose. The decomposition within $l = 0$, while not particularly informative on its own, is most useful for visualising other eigenspaces, because a projection onto the leading PCA mode in $l = 0$, $\mathbf{u}_0^{(l=0)}$, decodes a vorticity field resembling the laminar parallel flow solution. This field is invariant under all symmetry operations, allowing symmetries within the $l > 0$ eigenspaces to be identified.

A singular value decomposition within the $l = 1$ subspace reveals the presence of a large-amplitude leading mode, with higher order modes appearing in pairs at lower energies (see figure 8 in Methods). For visualisation of individual $l = 1$ modes we consider decodes of the projection with only the leading PCA mode from the $l = 0$ subspace included,

$$\bar{\omega}_n^{(1)} = \mathcal{D} (\mathcal{P}_0^0 + [\mathcal{P}_n^1 + \text{c.c.}]) . \quad (3)$$

As described above, the use of \mathcal{P}_0^0 alone removes much of the y -dependence when visualising $l = 1$ modes from projections of arbitrary snapshots due to the high degree of symmetry associated with $\mathbf{u}_0^{(0)}$. A specific example of this is included in figure 8 in Methods, and shows that the PCA modes within $l = 1$ decode structures which also have a number of discrete symmetries.

The large-amplitude primary PCA mode in the $l = 1$ subspace, $\mathbf{u}_0^{(1)}$, has a particular physical significance. Decoding projections $\bar{\omega}_0^{(1)}$ (equation 3) reveal a structure that is symmetric under rotation and shift-reflects, $\bar{\omega}_0^{(1)} = \mathcal{R} \bar{\omega}_0^{(1)}$, $\bar{\omega}_0^{(1)} = \mathcal{S}^m \bar{\omega}_0^{(1)}$ (see figure 8 in Methods) that strongly resembles the equilibrium born in the continuous-symmetry-breaking bifurcation off the laminar base state at low $Re \approx 10^{16,17}$. We explore this connection in figure 4, where we show that decodes of projections onto $\mathbf{u}_0^{(0)}$ and $\mathbf{u}_0^{(1)}$ can be used to reconstruct this structure over a *range* of Re , despite the fact that the training was conducted at fixed $Re = 40$. As the solution branch is traversed, the amplitude of the projection of the embedding onto $\mathbf{u}_0^{(1)}$ is increased. In the vorticity field, this corresponds to both a strengthening and tilting of the vorticity bands.

While it is surprising that this non-trivial, 2π -periodic equilibrium should form the backbone of the latent representations – neither it nor the laminar solution are seen explicitly during training – it is intuitive as further simple invariant solutions and the emergence of chaotic dynamics appear in bifurcations from this state. Note that this structure is associated with a *single* latent wavenumber, $l = 1$, in contrast to its physical Fourier transform which projects onto all physical wavenumbers.

The full structure of the state space of vorticity fields can be concisely visualised by first

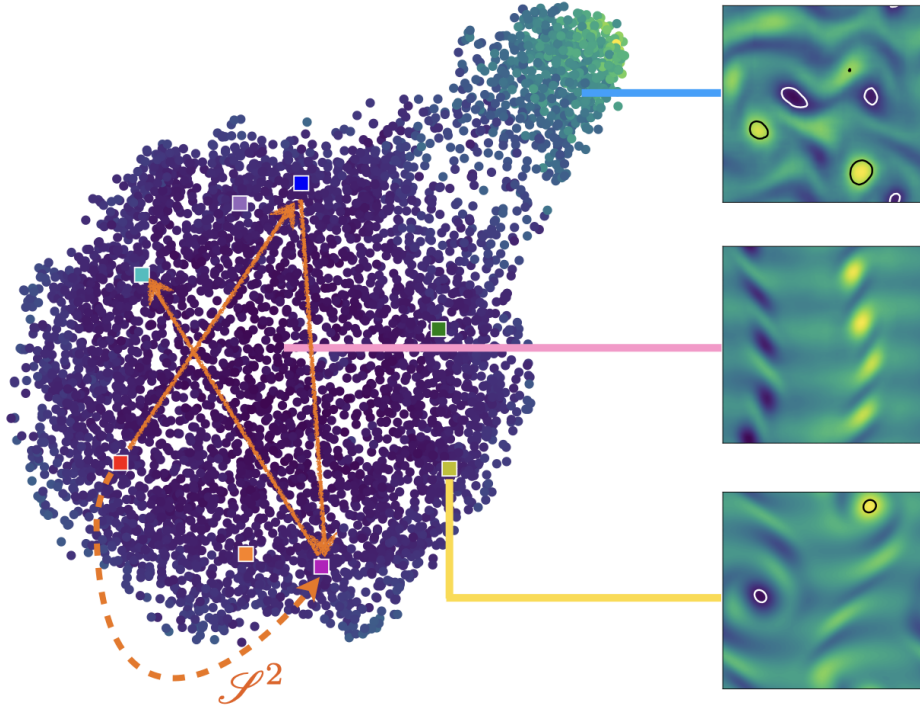


Figure 5: **Two-dimensional t-SNE of embeddings of 5000 vorticity snapshots in the $m = 96$ network.** The figure was created by computing projections of the embeddings onto the five leading PCA modes within each degenerate eigenspace $l \in \{0, 1, 2, 3\}$. Translational dependence of the features was then removed by taking the absolute value of these projections for $l > 0$ before the t-SNE algorithm¹⁸ was applied. The data points are coloured by their dissipation values which run between $D/D_l = 0.06$ (dark blue) and $D/D_l = 0.33$ (yellow). Decodes of example snapshots are shown on the right. The eight coloured squares represent the embeddings of the same vorticity snapshot (see the decode of the yellow square at bottom right) with the shift-reflect operation repeatedly applied. The orange arrows indicate how this field is moved between sectors of the low-dissipation octagon under applications of a shift-reflect operation; the dashed arrow labelled \mathcal{S}^2 corresponds to a full wavelength shift in y .

projecting embeddings of the test dataset onto the latent Fourier modes:

$$\psi(\omega) := \begin{pmatrix} \mathbf{u}_0^{0H} \mathcal{E}(\omega) \\ \mathbf{u}_0^{1H} \mathcal{E}(\omega) \\ \vdots \\ |\mathbf{u}_1^{0H} \mathcal{E}(\omega)| \\ \vdots \\ |\mathbf{u}_2^{0H} \mathcal{E}(\omega)| \\ \vdots \end{pmatrix}, \quad (4)$$

where the first five PCA modes each eigenspace are included, and taking the absolute value of projections onto PCA modes from eigenspaces $l \geq 1$ removes any dependence on the relative streamwise location of the recurrent patterns. A two-dimensional visualisation is then generated by supplying this observable as input to the t-SNE algorithm¹⁸. The output of this procedure is reported in figure 5, and shows a large octagon consisting of mainly low-dissipation embeddings and a detached high-dissipation cluster. Typically, the low-dissipation events require a single non-zero latent wavenumber, while the rarer, high-dissipation or ‘bursting’ snapshots have significant projections onto the $l = 2$ and $l = 3$ eigenspaces. This makes it clear that there is only a single class of ‘bursting’ event here, which is unlikely to be the case at higher Reynolds numbers.

Decoding example points from within the low-dissipation cluster reveals that its centre contains snapshots that are visually similar to the first equilibrium – compare the middle flow field in figure 5 to figure 4 – while embeddings of fields with pairs of opposite-sign vortices are situated towards the edges. The appearance of vortices which break the shift-reflect symmetry are indicative of secondary instabilities of the first equilibrium¹⁷. The eight sectors of the octagon-like cluster correspond to latent representations of the same recurrent patterns shift-reflected in the vertical direction. This effect is visualised in figure 5 by the square symbols in the cluster, which are eight copies of the embedding of the same vorticity field. This simple representation of the low-dissipation dynamics is retained in all autoencoders (even $m = 3$, not shown). Low- m networks do not build representations of the more complex bursting behaviour (see figure 1).

Finally, an important test of the physical significance of recurrent patterns is to show that they are particularly suited for identifying new simple invariant solutions. The quest to find a dynamical systems basis for turbulence has led to a search for such states which are invariably unstable and generically unstable periodic orbits (UPOs). This is typically done using *recurrent flow analysis*^{16,19–21} in which ‘near recurrences’ in a long turbulent time series are sought and then used as initial guesses in a Newton algorithm to converge simple invariant solutions of the Navier Stokes equations.

In the new approach using latent Fourier modes, near recurrences are flagged as local minima

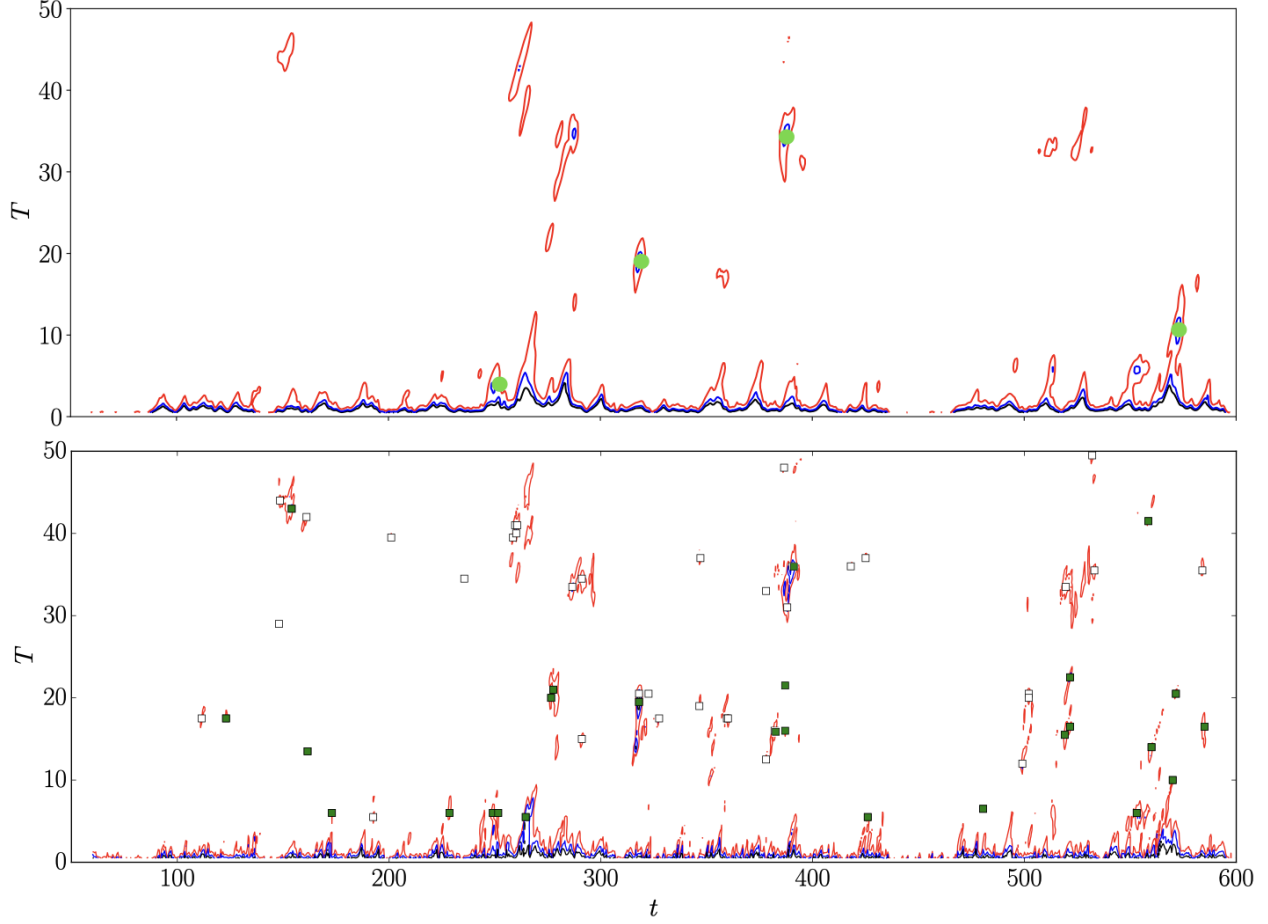


Figure 6: **Recurrent flow analysis using a Euclidean norm in physical space compared with one based on the latent observable ψ .** (Top) Measure R_ω (physical space). Contours indicate values of $R_\omega = 0.4$ (red), $R_\omega = 0.3$ (blue) and $R_\omega = 0.2$ (black). Local minima with values of $R_\omega < 0.4$ were supplied as guesses to the Newton solver; green dots indicate converged UPOs. (Bottom) Measure R_ψ (latent Fourier projections). Contours indicate values $R_\psi = 0.08$ (red), $R_\psi = 0.04$ (blue) and $R_\psi = 0.02$ (black). Local minima with $R_\psi < 0.08$ were supplied as guesses to the Newton solver; green squares indicate converged values.

below some threshold in

$$R_\psi(t, T) := \frac{\|\boldsymbol{\psi}(\omega(t)) - \boldsymbol{\psi}(\omega(t - T))\|}{\|\boldsymbol{\psi}(\omega(t))\|}, \quad (5)$$

built on the latent quantity $\boldsymbol{\psi}$ (equation 4) with the initial field $\omega(t)$ and guess for the period T then passed to the Newton solver (along with a shift s which can be determined from \mathcal{P}_0^1 , see Methods). We compare the number of guesses converged from minima in R_ψ to those converged based on the standard Euclidean norm in physical space,

$$R_\omega(t, T) := \min_s \frac{\|\omega(t) - \mathcal{T}_s \omega(t - T)\|}{\|\omega(t)\|}, \quad (6)$$

for an example time series in figure 6, with successful guesses marked. The measure based on $\boldsymbol{\psi}$ results in many more solutions; we have compared the performance of both measures over ~ 6000 time units, with R_ψ resulting in the discovery of around 22 UPOs per 1000 advective time units (8 unique) compared with 8 UPOs per 1000 advective time units (1/2 unique) for R_ω . Note that for 6000 time units, the ~ 50 unique UPOs found is roughly the same total identified in an analysis based on R_ω ($R_\omega < 0.3$) over 10^5 advective time units by Chandler & Kerswell¹⁶, which also included a search over discrete shifts in y .

Conclusion

In this paper we have used deep convolutional autoencoders to construct efficient low-dimensional representations of monochromatically forced, two-dimensional turbulence at $Re = 40$. The networks are highly effective at identifying recurrent spatial patterns in the vorticity field – common wavenumber pathways in a Fourier representation – in striking contrast with standard dimensionality reduction techniques. By exploiting a continuous symmetry we have developed an *interpretable* latent Fourier decomposition of the embeddings: the latent Fourier modes can be decoded into physically meaningful fields. At least one of these is clearly recognisable as a (non-trivial) unstable equilibrium of the system. This decomposition has also proved useful in establishing that the high-dissipation bursting events are of one type. Moreover, recurrent flow analysis based upon a latent observable in embedding space was found to be *much* better suited to identifying nearby simple invariant solutions than the standard Euclidean norm in physical space.

The results presented here clearly show that harnessing machine learning techniques to allow the building blocks of a flow representation to *design* themselves based on the flow dynamics is a significant step forward. The blocks which emerge are the principal spatial patterns or coherent structures observed in the flow and, intriguingly, can accurately capture simple invariant solutions embedded in the turbulent attractor without the solutions ever being realised precisely. This opens up the possibility of an easily automated, direct approach for both identifying when the flow is in the neighbourhood of a state in phase space and evaluating the probability of being there. Turbulent statistics could then be predicted through a weighted sum over relevant states, for example, in the

spirit of periodic orbit theory^{22,23}. However, in the immediate future, the natural next step is to apply these techniques at much higher Reynolds numbers and in three dimensions. In these extensions, assessing how much data is needed to power this approach will also be an important consideration.

Methods

Data. Training data are generated by solving equation (1) at fixed $Re = 40$. For spatial discretisation we apply a two-dimensional Fourier transform at a resolution $N_x \times N_y = 128 \times 128$; de-aliasing is applied according to the 2/3-rule. For timestepping, an implicit Crank-Nicholson scheme is employed for the diffusion term and Heun’s method is used for the nonlinear advection terms. For further details see Chandler & Kerswell¹⁶ and Lucas & Kerswell¹⁷.

The training dataset is constructed from 1000 independent trajectories each consisting of 100 snapshots separated by $\Delta t = 0.5$. Each trajectory was generated by simulating (1) from a randomly perturbed initial condition and discarding an initial transient. The vorticity fields are all normalized, $\omega_{\text{train}} = \omega/\omega_M$, where $\omega_M = 15$, which ensures $|\omega_{\text{train}}| < 1$. Each vorticity field then has a random symmetry transform applied $\omega \rightarrow \mathcal{T}_s \mathcal{S}^k \mathcal{R}^j \omega$ to ensure the network sees the full state space.

The test dataset used to generate the figures in this paper is constructed from a further 1000 trajectories in the same way.

Autoencoder architecture. The autoencoders discussed in this paper were all implemented using the Keras library²⁴. All share a common structure consisting of a series of five convolutional layers with periodic padding. The number of filters (and kernel size) decreases sequentially, $128(8, 8) \rightarrow 64(8, 8) \rightarrow 32(4, 4) \rightarrow 16(4, 4) \rightarrow 8(2, 2)$. Nonlinear ReLU activation is applied to the output of each layer. Each convolution is followed by a max pooling operation over regions of size 2×2 .

The convolutions are followed by three fully connected layers, all with ReLU activation, which run $128 \rightarrow m \rightarrow 128$. The fully connected layers are followed by a series of five convolutional layers which mimics the encoder described above, with up sampling applied after each convolution on patches 2×2 . A final convolutional layer with a tanh activation produces the output.

We trained networks with embedding dimension $m \in \{3, 8, 16, 32, 48, 64, 96, 128\}$. Training was performed for 800 epochs for batch sizes of 64 and 128 using an Adam optimizer with a learning rate of 0.001 or 0.0003. The results presented in this paper were generated using the best performing model at a given m . In order of increasing m these hyper parameters are (m , learning rate, batch size): (3, 0.001, 64); (8, 0.001, 128); (16, 0.001, 128); (32, 0.001, 128); (48, 0.0003, 64); (64, 0.0003, 128); (96, 0.0003, 64); (128, 0.0003, 128).

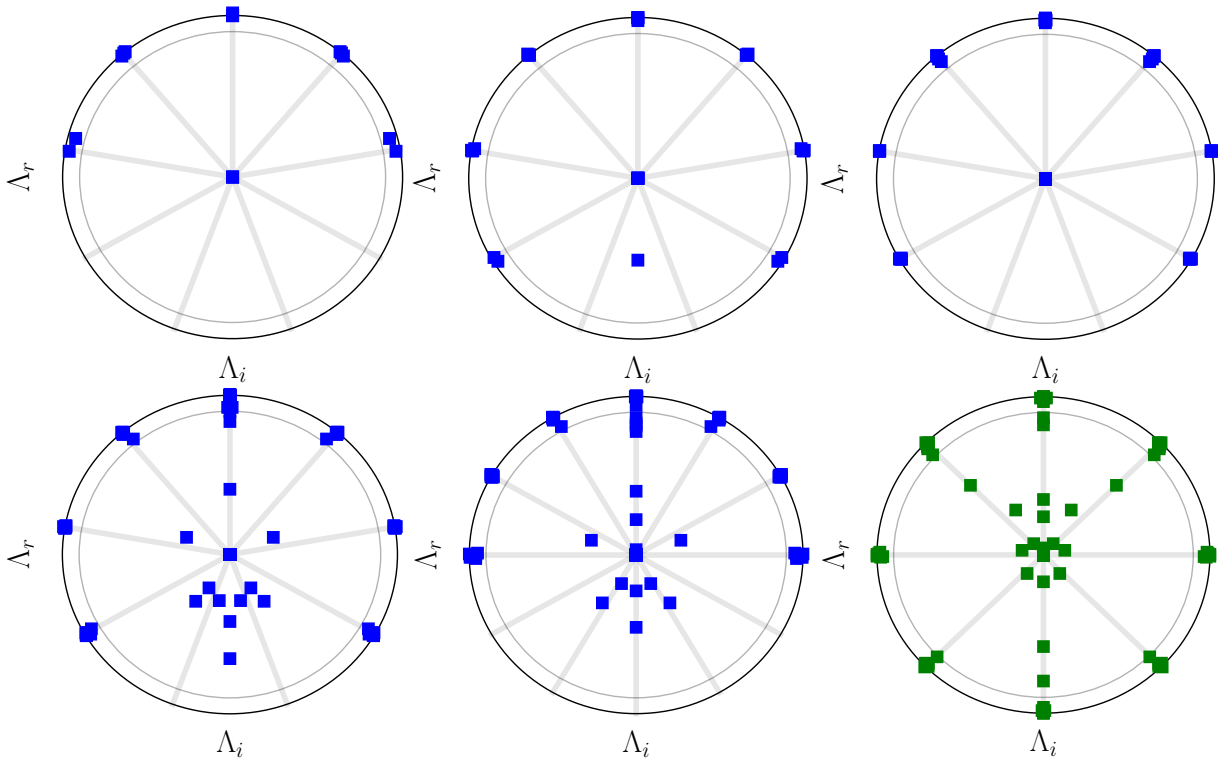


Figure 7: **Eigenvalue spectra of the latent symmetry operators for various embedding sizes m and shifts α .** (Top) Fixed $\alpha = 2\pi/9$; from left to right $m = 16, 32, 64$. (Bottom) Fixed $m = 96$. Left panel has $\alpha = 2\pi/9$, central panel $\alpha = 2\pi/12$. The final panel (green spectrum) shows eigenvalues of a numerical approximation to the vertical shift-reflect operator, \mathbf{S} . In all cases, the outer black circle is $|\Lambda| = 1$, the grey interior circle is $|\Lambda| = 0.9$. The rays from the origin identify the relevant roots of unity.

Details on symmetry operators. We construct shift operators \mathbf{T}_α for each network by first assembling a matrix of embeddings, $\mathbf{E} := [\mathcal{E}(\omega_1) \cdots \mathcal{E}(\omega_N)]$, along with another data matrix built from embeddings of the same vorticity fields shifted by α in x , $\mathbf{E}' := [\mathcal{E}(\mathcal{T}_\alpha\omega_1) \cdots \mathcal{E}(\mathcal{T}_\alpha\omega_N)]$. An approximate shift operator is then determined from a least-squares fit over the test set, $\mathbf{T}_\alpha = \mathbf{E}'\mathbf{E}^+$, where \mathbf{E}^+ is the Moore-Penrose pseudo inverse of \mathbf{E} . This algorithm is well-known in the fluid dynamics community, where it is typically applied to temporally-spaced flow snapshots to extract ‘dynamic modes’ with an exponential dependence on time ^{2,3,25}.

We compute a set of several shift operators in latent space, \mathbf{T}_α , for various network dimensions m and shifts α . The eigenvalue spectra of some of these operators are reported in figure 7 in ‘timestepper’ form. Latent wavenumbers can be extracted via $l = \Lambda/(i\alpha)$. At fixed α , the number of required latent wavenumbers saturates at $l = 3$ beyond $m = 32$. At fixed m , no further latent wavenumbers are recovered for shifts $\alpha < \pi/6$. Therefore, any shift $\alpha < \pi/6$ is sufficient to perform a latent Fourier transform without any aliasing issues.

The final spectrum reported in figure 7 (green symbols) corresponds to an operator that performs shift-reflect operations in the latent space,

$$\mathbf{S}\mathcal{E}(\omega) = \mathcal{E}(\mathcal{S}\omega). \quad (7)$$

The eigenvalues approximate the eight eighth roots of unity, as expected.

As discussed in the body of the paper, the latent wavenumbers $\{l\}$ are degenerate. Therefore, we are free to choose a basis with each eigenspace. We first construct an arbitrary bi-orthogonal basis from the numerically computed left- and right-eigenvectors of \mathbf{T}_α ,

$$\mathbf{\Xi}_l = \mathbf{V}_l\mathbf{R}^{-1}, \quad (8)$$

$$\mathbf{\Xi}_l^\dagger = (\mathbf{Q}^{-1}\mathbf{W}_l^H)^H, \quad (9)$$

where the columns of \mathbf{V}_l are the numerically computed right eigenvectors of \mathbf{T}_α corresponding to wavenumber l ; the columns of \mathbf{W}_l are the left eigenvectors. The matrices \mathbf{Q} and \mathbf{R} are the QR decomposition of $\mathbf{W}_l^H\mathbf{V}_l$. The columns of $\mathbf{\Xi}$ and $\mathbf{\Xi}^\dagger$ form a biorthogonal basis, $\mathbf{\xi}_i^\dagger\mathbf{\xi}_j = \delta_{ij}$. We then compute the projections of our test set of embeddings within each eigenspace, and perform PCA on the resulting data matrix to form an orthogonal basis ordered by ‘energy’.

As described in the body of the paper, visualisation of individual PCA modes associated with a particular latent wavenumber $l \geq 1$ also requires some contribution for the $l = 0$ eigenspace to be included in the decode. In the text we used only the leading PCA mode from this space (equation 3), though other choices are possible. For example, the full $l = 0$ subspace can be used,

$$\omega_n^{(1)} = \mathcal{D} \left(\sum_{j=0}^{d(0)-1} \mathcal{P}_j^0 + [\mathcal{P}_n^1 + \text{c.c.}] \right). \quad (10)$$

An example is included in figure 8, where we report the singular values in the $l = 1$ eigenspace and the decodes of projections onto individual PCA modes for an arbitrary snapshot using both

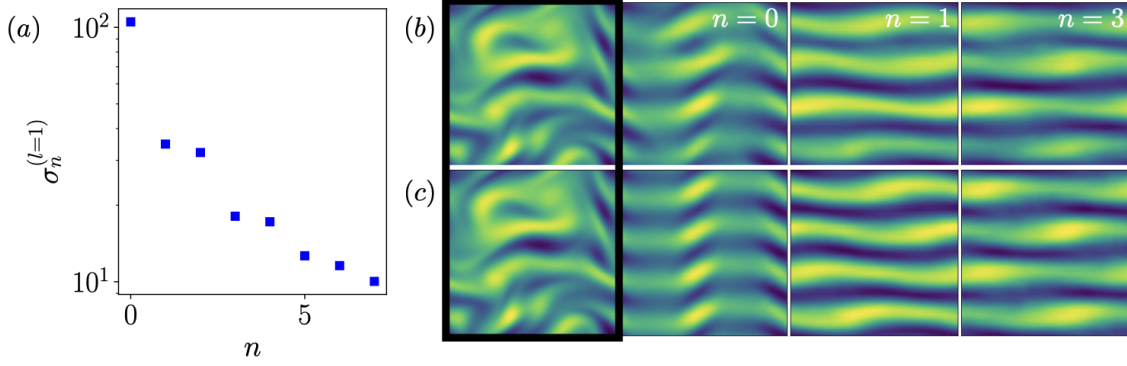


Figure 8: **Visualisation of the degenerate eigenspace $l = 1$ via decodes of projections onto its PCA modes for an example snapshot.** (a) Singular values from the $l = 1$ subspace. (b) An example vortical snapshot (left panel, highlighted with a black box) and the decode of the projection of its embedding onto *individual* PCA modes $\{\mathbf{u}_n^{(1)}\}$ within the $l = 1$ subspace, note the $l = 0$ projection is also included (see equation 10 in the text). (c) As (b) but only the first PCA mode from the $l = 0$ subspace is used (see equation 3 in the text).

equation (3) and equation (10). As noted in the main text, the leading PCA mode in $l = 1$ is revealed to be visually similar to the primary bifurcation of the flow at lower Re . Higher order PCA modes also have a large degree of discrete symmetry. For example, the slanted vortical structures associated with mode $\mathbf{u}_1^{(1)}$ are symmetric under rotation and whole-wavelength shifts, $\bar{\omega}_0^{(1)} = \mathcal{R} \bar{\omega}_0^{(1)}$, $\bar{\omega}_0^{(1)} = \mathcal{S}^{2m} \bar{\omega}_0^{(1)}$. The projection onto $\mathbf{u}_2^{(1)}$ (not shown) is simply the shift-reflect of $\mathbf{u}_1^{(1)}$, $\mathbf{u}_2^{(1)} = \mathcal{S}^{2m+1} \mathbf{u}_1^{(1)}$. The same set of symmetries hold for the vortex blobs obtained when decoding projections onto $\mathbf{u}_3^{(1)}$ and $\mathbf{u}_4^{(1)}$.

Unstable periodic orbits. Unstable periodic orbits (UPOs) correspond to solutions of (1) satisfying

$$\mathcal{T}_s \omega(\mathbf{x}, t + T) = \omega(\mathbf{x}, t). \quad (11)$$

In general these are *relative* periodic orbits as the recurrence is associated with a finite shift s in x – we have not here included the possibility of UPOs which also are shift-reflect in y . In our approach searches for UPOs are initialised using vorticity fields corresponding to local minima in the residual $R_\psi(t, T)$ (equation 5) rather than the standard Euclidean norm on ω which has been used previously. The guesses take the form (ω_g, T_g, s_g) : the vorticity field and period are known but the guess for the shift must be computed from the embedding (note the absolute values taken in the observable ψ remove any dependence on streamwise position). The projections of $\omega(t)$ and $\omega(t+T)$ onto the leading PCA mode in eigenspace $l = 1$ (which resembles the primary bifurcation of the flow under increasing Re) are used to generate a guess for the shift,

$$s_g = -i \log \left(\frac{\mathbf{u}_0^{(l=1)H} \mathcal{E}(\omega(t+T))}{\mathbf{u}_0^{(l=1)H} \mathcal{E}(\omega(t))} \right). \quad (12)$$

The guesses are input into a Newton-Raphson algorithm which has been described extensively in previous research^{16,21,26}. The size of the Jacobian matrix makes direct computation prohibitively expensive, and updates to the solution ($\delta\omega$, δT , δs) are instead computed within a Krylov subspace (Newton-GMRES) which requires computation only of the action of the Jacobian on a vector. A hookstep is used to constrain updates of the guess to within a specified trust region²¹.

References

1. Rowley, C. W. & Dawson, S. T. M. Model Reduction for Flow Analysis and Control. *Ann. Rev. Fluid Mech.* **49**, 387–417 (2017).
2. Schmid, P. J. Dynamic mode decomposition of numerical and experimental data. *J. Fluid Mech.* **656**, 5–28 (2010).
3. Page, J. & Kerswell, R. R. Koopman mode expansions between simple invariant solutions. *Journal of Fluid Mechanics* **879**, 1–27 (2019).
4. Landau, L. D. On the problem of turbulence. *Dokl. Akad. Nauk SSSR* **44**, 339–349 (1944).
5. Hopf, E. A mathematical example displaying features of turbulence. *Commun. Pure Appl. Math.* **1**, 303–322 (1948).
6. Kerswell, R. R. Recent progress in understanding the transition to turbulence in a pipe. *Nonlinearity* **18**, R17–R44 (2005).
7. Eckhardt, B., Schneider, T. M., Hof, B. & Westerweel, J. Turbulence transition in pipe flow. *Annual Review of Fluid Mechanics* **39**, 447–468 (2007).
8. Kawahara, G., Uhlmann, M. & van Veen, L. The significance of simple invariant solutions in turbulent flows. *Annual Review of Fluid Mechanics* **44**, 203–225 (2012).
9. LeCun, Y., Bengio, Y. & Hinton, G. Deep learning. *Nature* **521**, 436–444 (2015).
10. Gulshan, V. *et al.* Development and validation of a deep learning algorithm for detection of diabetic retinopathy in retinal fundus photographs. *JAMA* **316**, 2402–2410 (2016).
11. Pathak, J., Hunt, B., Girvan, M., Lu, Z. & Ott, E. Model-free prediction of large spatiotemporally chaotic systems from data: A reservoir computing approach. *Physical Review Letters* **120**, 024102 (2018).
12. Linot, A. J. & Graham, M. D. Deep learning to discover and predict dynamics on an inertial manifold. *Physical Review E* **101**, 062209 (2020).
13. Bar-Sinai, Y., Hoyer, S., Hickey, J. & Brenner, M. P. Learning data-driven discretizations for partial differential equations. *Proceedings of the National Academy of Sciences* **116**, 15344–15349 (2019).

14. Arnol'd, V. I. & Meshalkin, L. D. The seminar of A.N. Kolmogorov on selected topics in analysis. *Usp. Mat. Nauk* **15**, 247–250 (1960).
15. Platt, N., Sirovich, L. & Fitzmaurice, N. An investigation of chaotic Kolmogorov flows. *Physics of Fluids* **3**, 681–696 (1991).
16. Chandler, G. J. & Kerswell, R. R. Invariant recurrent solutions embedded in a turbulent two-dimensional Kolmogorov flow. *Journal of Fluid Mechanics* **722**, 554595 (2013).
17. Lucas, D. & Kerswell, R. Spatiotemporal dynamics in two-dimensional kolmogorov flow over large domains. *Journal of Fluid Mechanics* **750**, 518554 (2014).
18. van der Maaten, L. J. P. & Hinton, G. E. Visualizing high-dimensional data using t-SNE. *Journal of Machine Learning Research* **9**, 2579–2605 (2008).
19. Kawahara, G. & Kida, S. Periodic motion embedded in plane couette turbulence: regeneration cycle and burst. *Journal of Fluid Mechanics* **449**, 291300 (2001).
20. Cvitanovic, P. & Gibson, J. F. Geometry of the turbulence in wall-bounded shear flows: periodic orbits . *Physica Scripta* **T142**, 014007 (2010).
21. Viswanath, D. Recurrent motions within plane Couette turbulence. *Journal of Fluid Mechanics* **580**, 339358 (2007).
22. Artuso, R., Aurell, E. & Cvitanovic, P. Recycling of strange sets: I cycle expansions. *Nonlinearity* **3**, 325–359 (1990).
23. Artuso, R., Aurell, E. & Cvitanovic, P. Recycling of strange sets: II applications. *Nonlinearity* **3**, 361–386 (1990).
24. Chollet, F. Keras. <https://github.com/fchollet/keras> (2015).
25. Rowley, C. W., Mezić, I., Bagheri, S., Schlatter, P. & Henningson, D. S. Spectral analysis of nonlinear flows. *J. Fluid Mech.* **641**, 115–127 (2009).
26. Gibson, J. F., Halcrow, J. & Cvitanovic, P. Visualizing the geometry of state space in plane couette flow. *Journal of Fluid Mechanics* **611**, 107130 (2008).

Acknowledgements JP acknowledges support from the Sultan Qaboos Fellowship at Corpus Christi College, University of Cambridge. MPB acknowledges support from the Simons Foundation and also from NSF Division of Mathematical Sciences grant DMS1715477.

Author Contributions The project was conceived and developed by all three authors who also contributed significantly to the writeup. JP did the majority of the computations with help from MPB.

Competing Interests The authors declare that they have no competing financial interests.

Correspondence Correspondence and requests for materials should be addressed to J. Page (email: Jacob.Page.ed.ac.uk).